Graphdiyne interface engineering: highly active and selective ammonia synthesis

Yan Fang[1], Yurui Xue[1]*, Yongjun Li[1]*, Huidi Yu[1], Lan Hui[1], Yuxin Liu[1], Chengyu Xing,[1] Chao Zhang[1], Danyan Zhang[1], Zhongqiang Wang[1], Xi Chen[1], Bolong Huang[2]*, and Yuliang Li[1,3]*

Abstract

A freestanding 3D graphdiyne-cobalt nitrides (GDY/Co_2N) with highly active and selective interface is fabricated for electrochemical nitrogen reduction (ECNRR). This interface is rationally designed and constructed under the inspiration of function orientation. The GDY contributes a unique p-electronic character to optimally modify the Co-N compound surface bonding and promote the cobalt species to high valence states, which generates as-observed superior electronic activity for ECNRR catalysis. Density functional theory (DFT) calculation results show that the strong interfacial p-d correlation indicates an efficient electron-transfer with minimizing ECNRR barrier. Our results indicated that the electrocatalyst creates a new record of synthetic ammonia yield and faradaic efficiency with a high ammonia yield rate (Y_{NH3}) of 219.72 μg h^{-1} $mg_{cat.}^{-1}$ and Faradaic Efficiency (FE) of 58.60 % in acidic media at atmospheric pressure and room temperature that are higher than previously reported any electrocatalysts. As a novel electrocatalyst promising to generate new concepts, new knowledge, and new phenomena in electrocatalytic research, our work is beneficial in driving rapid development in the field of electrocatalysis.

[1]Institute of Chemistry, Chinese Academy of Sciences, Beijing 100190, P. R. China. [2]Department of Applied Biology and Chemical Technology, The Hong Kong Polytechnic University, Hung Hom, Kowloon, Hong Kong SAR, P. R. China. [3]University of Chinese Academy of Sciences, Beijing 100049, P. R. China. *e-mail: xueyurui@iccas.ac.cn, liyj@iccas.ac.cn, bhuang@polyu.edu.hk, ylli@iccas.ac.cn

Introduction

The emergence of synthetic ammonia has changed the food of billions of people in the world. Therefore, the research of synthetic ammonia, especially at room temperature and atmospheric pressure, has been the focus of great attention of chemists. The electrically catalyzed reduction of nitrogen to the carbon-free ammonia (NH_3, $N_2 + 6H^+ + 6e^- \rightarrow 2NH_3$) under ambient conditions is a promising alternative to the energy- and carbon-intensive Haber-Bosch process ($N_2 + H_2 \rightarrow 2NH_3$) that is widely used in industrial NH_3 production at high pressures and temperatures (200 atm, 400 – 450 °C, iron catalyst)[1-4] In order to avoid the harsh synthetic conditions and serious pollution caused by the above synthesized ammonia route, the most critical of the synthetic ammonia process is the synthesis of highly selective and efficient catalysts to activate the inert N≡N bond of nitrogen (N_2) and the NH_3 synthesis at ambient conditions. At present, a variety of ECNRR electrocatalysts, such as nitrides[5,6], sulfides[7], oxides[8,9], etc., have been successively used for the synthesis of NH_3[6,7,9-13]. and their catalytic performances, ammonia yield (Y_{NH3}), Faradaic efficiency (FE) are still low and the application potential is very deficient. Therefore, the promoted development of the synthetic ammonia industry is necessary to subvert the development of excellent electrocatalysts with comprehensive properties and break the bottleneck of the development of high yield rate and the selective synthesis ammonia at ambient conditions.

The 3d-transition-metal (TM) based materials have shown the advantages for N_2 activation via the “acceptance-donation” interaction mechanism between the TM and N_2. Such an interaction mechanism is beneficial to the ECNRR process. However, until now, the study of 3d-transition-metal-based materials as efficient ECNRR catalysts, there is still no widespread concern. Homogeneous catalysts (molecular catalysts) is considered to have great potential for selective nitrogen reduction under ambient conditions[14,15]; their low stability and yield are also not suitable for their low stability and yield are also not suitable for high-efficiency

electrocatalysis. Heterogeneous catalysts, feature high stability toward ECNRR under ambient conditions and can be easily equipped with energy-conversion devices; but they suffer from the competition between ECNRR and hydrogen evolution reaction (HER) causing serious selectivity loss[10]. Based on the above analysis, catalysts with high selectivity, high efficiency, high Y_{NH3} and high stability were not found so far. In recent year, the high-speed development of science and technology, and the unique glamour of high-end instruments and equipment in the characterization of catalyst, lead to the best period of catalyst development. In view of the important scientific problems in this field, through the understanding of the composition, structure, surface structure, surface transportation and the regularity of these behaviors and properties of catalysts, it is the only way to find out the catalyst with high efficiency and excellent comprehensive performance. In the light of the above, we propose electrocatalytic reactions to have more advantages in kinetics and thermodynamics, which are beneficial to new electrocatalytic systems. Incorporating metal catalysts with carbon materials to form elaborately engineered interface is an important approach for improving the selectivity, activity and efficiency of electrocatalysts. Among all carbon materials, Graphdiyne (GDY), possessing unique porous structure, uneven-distributed surface charge, (electro)chemical stability and high conductivity, has received increasing interests on its versatile applications in catalysis, energy conversion and storage, etc.[12,16-25]. Especially, the GDY can be grown in-situ on arbitrary supports, generating engineered interfaces with improved charge transfer, increased active site numbers, and enhanced long-term stability. These fascinating properties of GDY makes it more active and efficient than conventional carbon materials. Previous reports[18,20,22,26-32] have demonstrated that the GDY could provide great amounts of active sites and substantially enhance the overall catalytic activities and stabilities in the electrocatalysis. Rational design of GDY-based materials as ECNRR catalysts would lead to a new class of catalysts for practical applications.

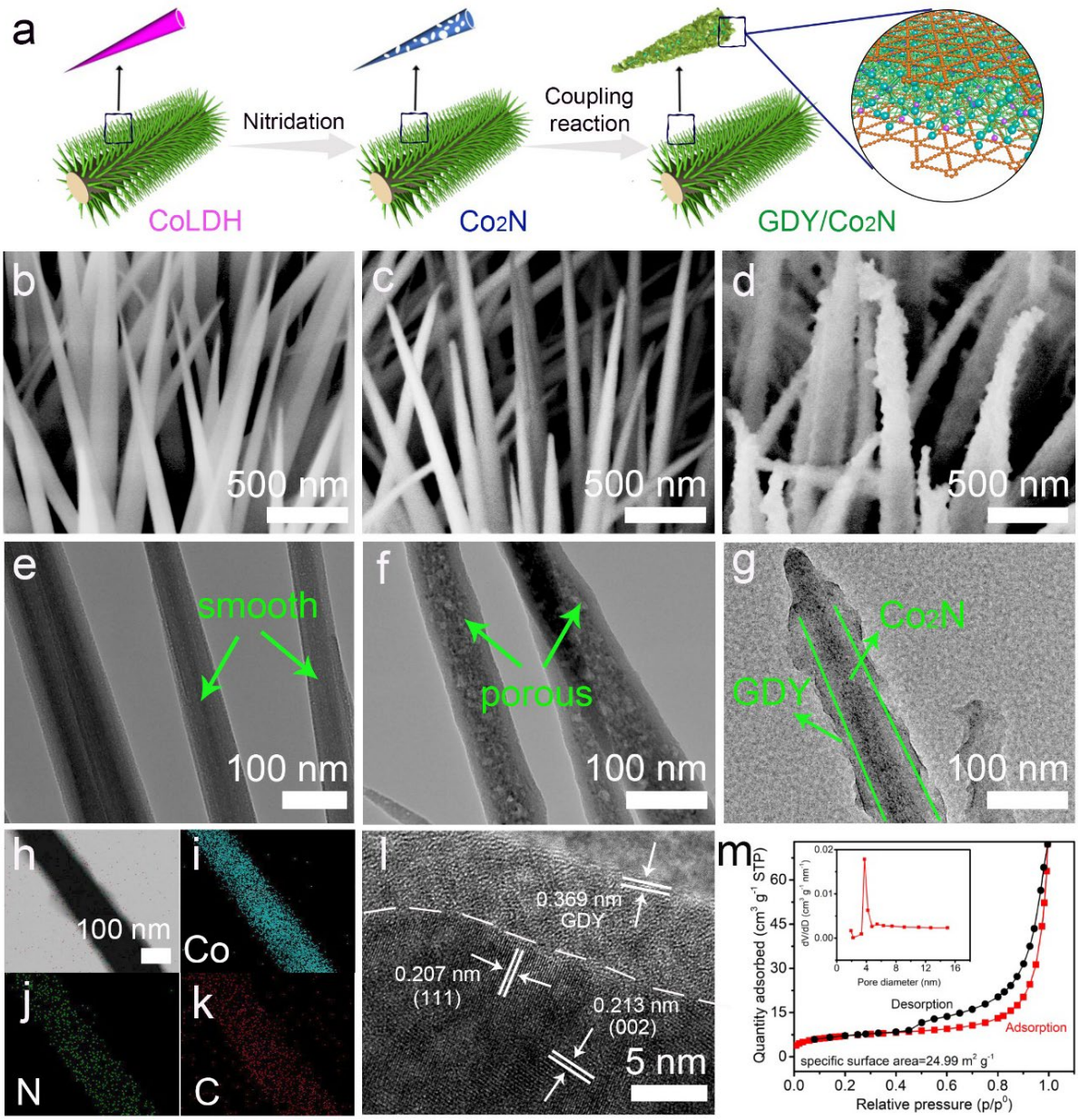

Fig. 1 | Morphological characterizations. a, Schematic illustration of the preparation of self-standing GDY/Co_2N. **b**, SEM image of CoLDH. **c**, SEM image of Co_2N. **d**, SEM image of Co_2N/GDY. **e**, TEM image of CoLDH. **f**, TEM image of Co_2N. **g**, TEM image of GDY/Co_2N. **h-k**, EDX elemental mapping results of GDY/Co_2N. **l**, HRTEM image of Co_2N/GDY. **m**, Adsorption and desorption isotherm of GDY/Co_2N (inset: pore size distribution of GDY/Co_2N).

During our preliminary rough screening, Co_2N has been identified as the stable and potential electrocatalyst for NRR. Meanwhile, this also supports the nitrides as widely used electrocatalyst in the NRR experiments. In this work, we report the facile and scalable synthesis of self-standing cathode by in-situ growing graphdiyne nanosheet arrays (GDY

NAs) on the surface of cobalt-nitride nanowires (Co_2N NWs) grown on carbon cloth (GDY/Co_2N NWs, Fig.1a). With interface bonding modification, the interface Co-sites indicate an electron-pumping like character for depleting the electrons from Co_2N towards GDY layer. We found that the 3D self-standing GDY/Co_2N cathode features the high selectivity and efficiency for NH_3 synthesis at ambient pressures and room temperatures in both acidic and neutral conditions. Especially, in 0.1 M HCl (pH = 0) condition, it can achieve the highest Y_{NH3} and FE of 219.72 μg h^{-1} $mg_{cat.}^{-1}$ and 58.60% at a low potential of –0.2 V, outperforming previously reported ECNRR catalysts. Besides, it also exhibits high Y_{NH3} and FE. Moreover, such excellent catalytic performances can be maintained over 114 and 144 h in acidic and neutral conditions, respectively. Our results demonstrate that the superior electronic activity of ECNRR catalysis at the interface region arises from the unique GDY electronic character. DFT calculation results suggest that the anomalous decreasing of d-to-pσ* state transition minimizes the barrier of N_2-fixation for reaching the optimal ECNRR initiation. These are the key promotion for high electronic activities and ECNRR performance simultaneously.

Results and Discussion

Morphological characterizations. As shown in Fig.1a, the porous Co_2N nanowires (p-Co_2N NWs) were prepared by nitriding the freestanding CoLDH nanowires through a facile hydrothermal method. It can be seen that the nitridation treatment introduces numerous of pores and defects throughout the nanowire (Fig.1e and f). Using p-Co_2N NWs as supports, graphdiyne nanosheet arrays (GDY NAs, Fig.1d) were chemically grown on the p-Co_2N NW surface by the coupling reaction (GDY/Co_2N). The scanning electron microscopy (SEM, Fig.1d) and transmission electron microscopy (TEM, Fig.1g) images show that the nanowire-morphology was well preserved while the nanowire surface was roughened during the GDY growing process (average size of the pores is around 5.4 nm, Fig.1m). The surface area also increases from 18.08 (p-Co_2N NWs, Supplementary Fig.2) to 24.99 m^2 g^{-1} (GDY/Co_2N NWs,

Fig.1m). The TEM (Fig.1g) and scanning TEM (STEM, Fig.1h) images evidenced the core-shell structure of the GDY/Co_2N nanowire. The intimate interface between the p-Co_2N and GDY could be clearly seen by using the STEM and HRTEM measurements. Energy-dispersive X-ray spectroscopy (EDX) elemental mapping results (Fig.1i-k) indicate the Co and N are homogeneously distributed only in the core region of the nanowire, while the C element distributed over the whole width of the nanowire. Fig.1l clearly showed that the p-Co_2N has lattice spacing of 0.213 and 0.207 nm corresponding to the (002) and (111) facets in accordance with X-ray diffraction (XRD) results (Supplementary Fig.3a), covered by an amorphous GDY film (fringe spacing: 0.369 nm; the average thickness: ~ 6.0 nm). The fringe spacing of the Co_2N and GDY species become smaller than their pure ones, indicating the synergistic interactions between these two components. These indicated the strong interaction between GDY and p-Co_2N that would greatly facilitate the charge transfer behavior and enhance the conductivity of the catalyst, in accordance with the XPS, Raman and XANES results as discussed later.

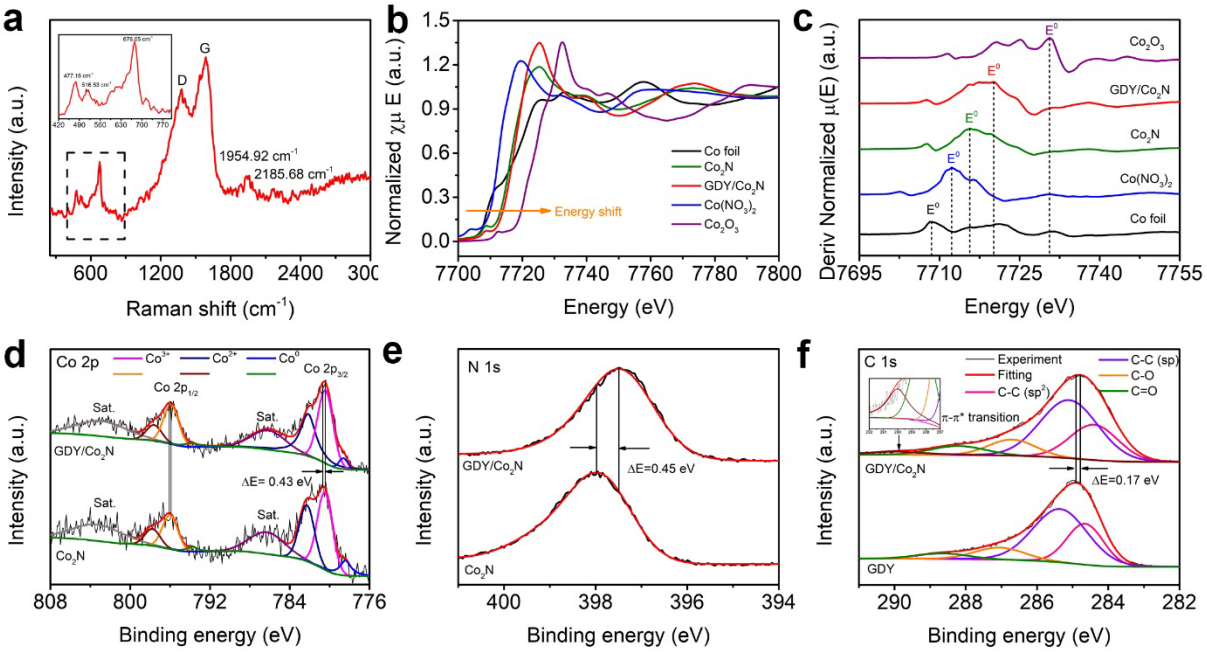

Fig. 2 | Structural characterizations. a, Raman spectroscopy of GDY/Co_2N (inset: characteristic peaks of Co_2N). **b**, The normalized Co K-edge XANES spectra of samples. **c**, First-derivative curves of XANES of samples. **d**, The Co 2p XPS spectrum of GDY/Co_2N and

Co_2N. **e**, The N 1s XPS spectrum of GDY/Co_2N and Co_2N. **f**, The C 1s XPS spectrum of GDY/Co_2N and pristine GDY.

Activity Analysis. The nature defects of the samples were analyzed by Raman spectroscopy. Fig.2a shows the Raman spectrum of the GDY/Co_2N has three dominant peaks at 477.16, 516.53, and 676.05 cm^{-1} corresponding to Co_2N species (Supplementary Fig.5), and four peaks at 1373.21 (D band), 1586.28 (G band), 1954.92 and 2185.68 cm^{-1} (vibrations of the conjugated diyne links) corresponding to GDY species (Supplementary Fig.5**)**. It is observed that the intensity ratio of the D and G band (I_D/I_G) increased from 0.75 (GDY) to 0.92 (GDY-Co_2N), which confirms that the defect number increased after the GDY growth implying the substantial binding of the GDY/Co_2N interfacial region. The above results demonstrate the successful synthesis of GDY/Co_2N.

The electroactivity of chemical components within the surface/interfaces was further studied by using X-ray photoelectron spectroscopy (XPS), X-ray absorption near edge structure (XANES) and extended X-ray absorption fine structure (EXAFS). The C 1s XPS spectrum of GDY/Co_2N (Fig.2f) exhibits five peaks corresponding to sp^2-C (284.4 eV), sp-C (285.1 eV), C-O (286.7 eV), C=O (288.2 eV) and π-π* transition (290 eV), respectively. The presence of π-π* transition peak verifies the interaction between GDY and Co_2N[20,24,33]. As shown in Fig.2d the Co 2p spectra show two spin-orbit triplets at 780.43, 782.14 and 778.62 eV and at 796.02, 797.71 and 793.72 eV as well as two shakeup satellite at 786.34 and 802.90 eV, respectively. The triplets have been assigned to Co^{3+}, Co^{2+} and Co^0 species, respectively. Compared with the pristine Co_2N, the Co 2p spectrum of GDY/Co_2N shifts to higher binding energy by 0.43 eV (Fig.2d**)** while the N 1s spectra shifts to lower binding energy by -0.45 eV (Fig.2e**)**, revealing the obvious electron charge transfer between Co_2N and GDY. More Co^{3+} species were generated after GDY growth, suggesting Co atoms shift to a higher valence state in the interface. The XANES and EXAFS were further performed to determine the chemical states of the samples. The Co K-edge XANES spectra (Fig.2b) of GDY/Co_2N show the

increases of the edge and main peak energies compared to Co_2N. The E^0 peak in the first-derivative curves of XANES of the GDY/Co_2N (Fig.2c) also located at higher binding energies than that of Co_2N and $Co(NO_3)_2$, but lower than that of Co_2O_3. These indicate that the proportion of the Co atoms with higher valence in GDY/Co_2N is higher than that of Co_2N. As previously reported, the Co atoms at higher valence are proposed to be more catalytically active in electrocatalysis[34,35].

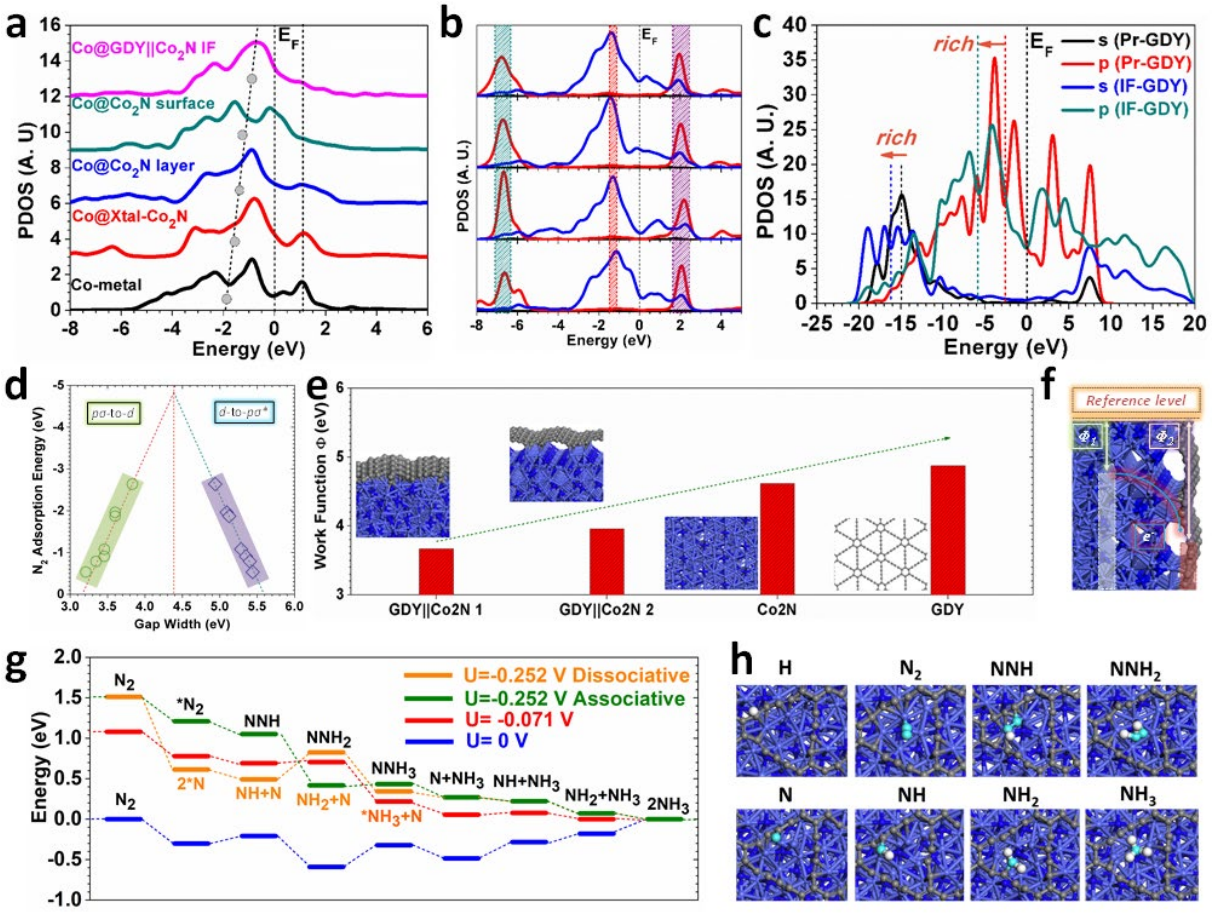

Fig. 3 | Electronic activities and energetic pathways of GDY||Co_2N for ECNRR catalytic activity. **a**, Site-dependent PDOSs of Co-3d band variation from in-depth Co_2N towards interface region, with compared to Co-metal state. **b**, Relative position alignment of p-d band between active interfacial Co-sites and adsorbing N_2. **c**, PDOSs Comparison for GDY between cases of free-standing and interface bonded. **d**, Volcano-like correlation between electron-transfer gap and N_2-adsorption energy. **e**, Work function comparison among different interface and surface systems. **f**, Schematic electron-transfer path driven by the work-function differences and p-d orbital correlation. **g**, Reaction pathway of acidic NRR catalysis at the

potential of U=0 V, U=-0.071 V, and U=-0.252 V. **h**, The local structural configurations for demonstrating the ECNRR (acidic) process within the GDY||Co_2N surface system.

We reasoned the high NRR performance from DFT calculations. The GDY shows less surface mismatching effect with Co_2N (111) compared with other directions. However, certain strain effects have been induced by the interface (IF) bonding between GDY and Co_2N surface, which induces surface reconstructions and various lattice distortions. This implies the Co-sites play an active role for bonding with GDY layer (Supplementary Fig. 7a-7c). The bonding and anti-bonding orbitals near Fermi level (E_F) have been demonstrated. The GDY layer has been clearly shown an electron-rich character, which indicates an electron-transfer trend from Co_2N towards GDY layer (Supplementary Fig. 7d). Site-dependent Co-3d band center variation trend exhibits a near-linear trend of uprising towards E_F, from E_V-1.9 eV for the bulk Co-metal towards E_V-1.0 eV for the Co-site at the IF, respectively. Meanwhile, the e_g-t_{2g} splitting effect has been minimized where the e_g-component above E_F downshifts and merges with t_{2g} orbital staying near E_F (Fig. 3a). We selectively demonstrate the 3d-bands of interfacial Co-sites and N_2-2p orbitals for stable N_2-adsorption. We confirm that the Co-sites are electronic active for charge transfer from Co-3d to the empty-state of N_2-2p orbital (pσ*), facilitating the N_2-stabilization (Fig. 3b). We compared the 2p-orbital behavior between the interface bonded and pristine GDY layers, where the C-2p orbital overall indicates an energetic downshift of 2.5 eV. Such a trend enhances the $N \equiv N$ electronegativity for capturing H^+ instead of the H^+-electron-exchange (Fig. 3c). Meanwhile, for those N sites bonding with Co atoms, N-2p orbitals have been gradually pushed towards the lower position from the surface sites to the interfacial region and become more electron-rich. This is highly consistent with the lower binding energy in experimental XPS results (Supplementary Fig.7e).

According to the above discussed electron-transfer enhanced N_2-fixation, we further correlate the p-d coupling and the N_2-adsorption. There has been a volcano-like correlation discovered. This correlation tells a trend that, the interface-bonding modification promotes the

electron-transfer from Co-3d band on the Co_2N surface towards the empty pσ*-orbitals of N_2 for stable chemical adsorption, for preventing early stage of N≡N bond cleavage (Fig. 3d). From the initial N_2 adsorption to the final desorption of NH_3, we observe the two consecutive linear correlations within the position of the dominant peak of N-2p orbitals during NRR. The N-containing species gradually becomes more electron-rich as the formation of ammonia. For the generation of each NH_3, the electronic linear correlation is the pivotal factors for actualizing efficient NRR with the associative mechanism (Supplementary Fig. 7f). In addition, the highly active inter-layer bonding enhances the electron-transfer between Co_2N and GDY layers. From the work function comparison among different systems, it reflects that stronger interface bonding between GDY and Co_2N exhibits a lower work function for transferring electrons towards adsorbing N-species (Fig. 3e). Schematic picture shows that, the Co_2N layer plays as an electron-pumping center for maintaining the electron-rich character for GDY at higher electronegative level (Fig. 3f).

Further viewing on energetic trend of ECNRR pathway, we find the reaction-heat shows an overall energetic gain at -1.51 eV and energetic favorable with most steps in downhill trend. The overall energetic gain has been further transformed into the electrode potential between -0.071 V and -0.252 V, which show a good agreement with experimental measurement. The dominant barrier at U=-0.252 V is denoted at the step of forming $*N_2H_3+3(H^++e^-)$ from $*N_2H_2+4(H^++e^-)$, which is only 0.13 eV at the U=0 V (Fig. 3g). For the dissociation mechanism under the same applied potential of U = -0.252 V, the reaction pathway still displays a large barrier of 0.33 eV at the formation of the first ammonia, indicating the low preference of the dissociation mechanism for ECNRR. Meanwhile, the competitive HER process on Co_2N/GDY is not energetically favorable due to the high barrier of 0.539 eV for chemisorption of H, which significantly suppresses the further HER process. Moreover, the barrier of chemisorption of HER also demonstrates the H overbinding effect has been

alleviated, supporting efficient hydrogenation within ECNRR (Supplementary Fig. 7g). From local structural configurations (Fig. 3h), we find all N-species are energetically favorable adsorbing on the lower coordinated Co-site stably bonded by GDY layer, while the nearby C-sites with alkyne bond plays an enhanced electron-proton exchange center for re-distributing the H-species representing a rather high selectivity.

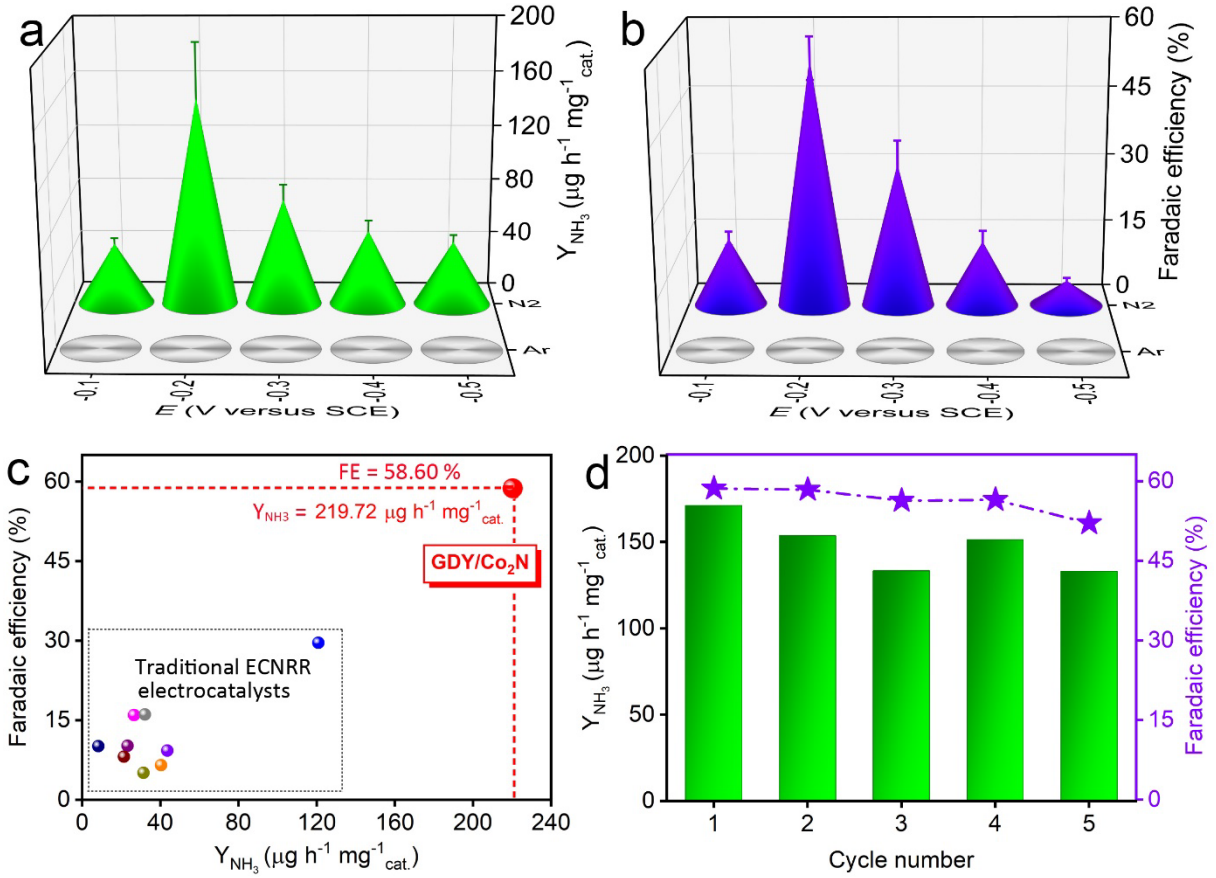

Fig. 4 | Acidic ECNRR performances. a, Y_{NH3} of GDY/Co_2N at different potentials in N_2- and Ar-saturated 0.1 M HCl (bars represent standard deviation). **b**, FEs of GDY/Co_2N at different potentials in N_2-and Ar-saturated 0.1 M HCl (bars represent standard deviation)**. c**, Y_{NH3} and FEs of GDY/Co_2N and some reported excellent electrocatalysts performed in acid conditions. **d**, Cycling test of GDY/Co_2N at -0.2 V versus SCE in 0.1 M HCl.

Electrochemical performances. The electrochemical measurements were firstly performed in 0.1 M HCl in a two-compartment cell separated by Nafion 117 membrane. Freshly prepared samples, saturated calomel electrode and graphite rod were used as the working electrode, the reference electrode and the counter electrode, respectively. The ECNRR is operated in the N_2 atmosphere (1 atm) with N_2 gas continuously being supplied at

the cathode and protons transporting from the electrolyte to the catalyst. NH_3 was then synthesized on GDY/Co_2N surface during the reduction reaction process and protonated in the electrolytes forming NH_4^+, which could be determined by the spectrophotometry method (Supplementary Fig.8 and Fig.14)[12]. The possible by-product hydrazine was detected by the Watt–Chrisp method (Supplementary Fig.9)[36]. Linear sweep voltammetry (LSV) curves recorded in N_2- and Ar-saturated 0.1 M HCl aqueous solution clearly revealed the occurrence of the efficient ECNRR (Supplementary Fig.10a). The UV-vis adsorption curves and the chronoamperometry curves recorded at different potentials were shown in Supplementary Fig.10b-c, respectively. The electrolyte obtained at –0.2 V exhibits the highest absorbance intensity. Fig.4a-b displays the average NH_3 yield (Y_{NH3}, with standard deviation) and corresponding Faradaic efficiencies (FEs, with standard deviation) at different potentials. At the applied potential of -0.2 V versus SCE, GDY/Co_2N exhibits the ECNRR performances with the Y_{NH3} of 151.24 ± 38.50 μg h^{-1} $mg_{cat.}^{-1}$ and FE of 53.82 ± 4.57 % (Fig.4a-b and Supplementary Table 3). The highest values of Y_{NH3} and FE reach up to 219.72 μg h^{-1} $mg_{cat.}^{-1}$ and 58.60%, respectively, which are higher than previously reported ECNRR electrocatalysts ((Fig.4c) such as B_4C[37], a-Au/CeO_x-RGO[11], FL-BP NSs[38] and VN[5] (please see Supplementary Table 5 for more comparisons). UV-vis spectra for detection of N_2H_4 showed no peak in 455 nm (Supplementary Fig.10d), verifying no by-product formation during NRR process. To verify that detected NH_3 was originated from the reduction of N_2 by GDY/Co_2N, the electrolysis was performed in Ar-saturated electrolytes at all applied potentials. As shown in Supplementary Fig.11, no signals could be seen from the UV-Vis spectra, which indicates that no NH_3 was formed (Fig.4a-b), demonstrating that the high reaction selectivity of our catalyst. ^{15}N isotopic labeling experiment was also performed to determine the N source of the produced ammonia. As shown in Supplementary Fig. 19a, the ^1H NMR signal for $^{15}NH_4^+$ was detected after ECNRR under 0.1 M HCl condition using $^{15}N_2$ as the feeding gas. The spectrum showed that the characteristic peak for $^{15}NH_4^+$ was split by the nuclear spin of ^{15}N

into a well-known doublet in the range of 6.85-7.15 ppm, in consistent with the reported works[refs].These results confirm the NH_3 was really produced from the N_2 reduction but not the N element of Co_2N species. We further investigated the origin of the ECNRR abilities of GDY/Co_2N. As shown in Supplementary Fig.12b, the CF substrate and Co_2N presented low Y_{NH3} of only 0.08 and 14.83 μg h^{-1} $mg_{cat.}^{-1}$, which are much smaller than that of GDY/Co_2N. According to the above discussion, the incorporation of GDY and Co_2N can effectively enhance the ECNRR ability of an electrocatalyst towards more efficient N_2 reduction electrocatalysis.

Besides activity and selectivity, stability is another important factor for ECNRR electrocatalysts. The Y_{NH3} and FE of GDY/Co_2N exhibited slight decrease after 5-cycle ECNRR tests (Fig.4d). Besides, the GDY/Co_2N shows almost no variation in the current density during the 114 h continuous electrolysis (Supplementary Fig.13a). The XRD (Supplementary Fig.20) and SEM (Supplementary Fig.21) measurements reveal that no obvious changes in the crystalline and the morphologies of the GDY/Co_2N obtained after stability tests, demonstrating the morphological and structural stability of our electrocatalyst. The Co 2p, N 1s, O 1s and C 1s XPS spectra of GDY/Co_2N suggested that more Co^{3+} species were generated and the surfaces of Co_2N partially transferred to oxide species during a long-time electrocatalysis (Supplementary Fig.22). The ECNRR performances of the samples were further studied in neutral electrolyte (0.1 M Na_2SO_4). GDY/Co_2N achieves the highest Y_{NH3} and FE of 123.66 μg h^{-1} $mg_{cat.}^{-1}$ and 35.84%, respectively at -0.6 V versus SCE (Fig.5a-b), which are higher than Co_2N (Y_{NH3} = 13.22 μg h^{-1} $mg_{cat.}^{-1}$, FE = 5.11%) and the reported ones, such as Pd/C[39], Mo_2C/C[40], DR MoS_2[41], and MHCMs[42], measured in neutral conditions, revealing the excellent catalytic activity of the GDY/Co_2N. As expected, no NH_3 could be detected in Ar-saturated 0.1 M Na_2SO_4 (Supplementary Fig.16 and Fig.5a-b). Two resonance peaks for $^{15}NH_4^+$ were also obtained in the ^1H NMR analysis after ECNRR in 0.1 M Na_2SO_4 using $^{15}N_2$ as the feeding gas (Supplementary Fig. 19b), evidencing the NH_3 was also

synthesized by reducing the nitrogen gas in neutral conditions. No N_2H_4 by-product could be detected at all applied potentials in N_2-saturated electrolytes (Supplementary Fig.15d), confirming the high selectivity of the GDY/Co_2N towards the ECNRR electrolysis. Moreover, the GDY/Co_2N exhibits high long-term stability with 87.68% and 71.02% retention of the Y_{NH3} and FE, respectively, after 7 times recycling tests (Fig.5d). And there is negligible decrease in the current density during a 144-hour electrocatalysis (Fig.18a). XRD (Supplementary Fig.23) and SEM (Supplementary Fig.24) measurements exhibited the well-retained crystalline structure and morphology after 7 times ECNRR tests. XPS results after cycling test also revealed the formation of cobalt oxides during ECNRR, which was similar to that in acid conditions (Supplementary Fig.25).

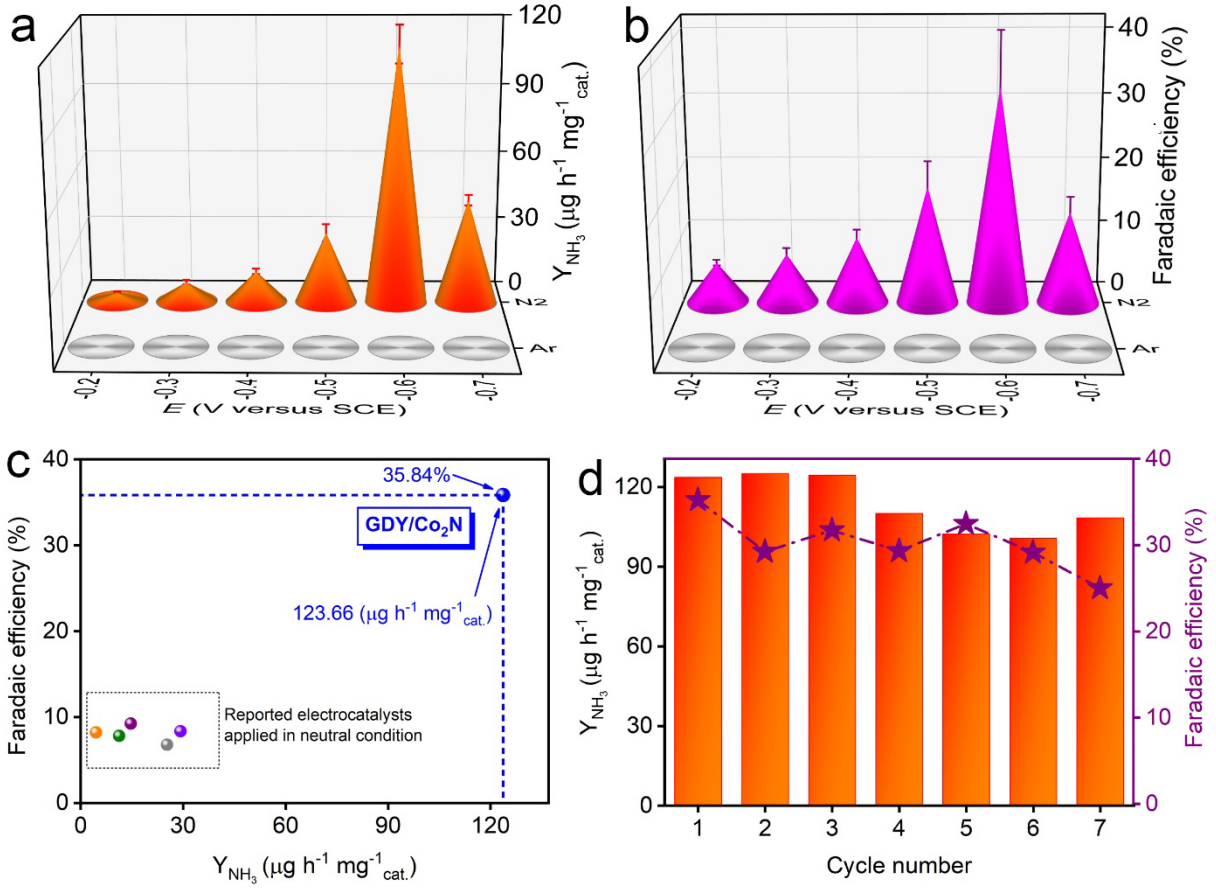

Fig. 5 | Basic ECNRR performances. a, Y_{NH3} of GDY/Co_2N at different potentials in N_2-and Ar-saturated 0.1 M Na_2SO_4 (bars represent standard deviation). **b**, FEs of GDY/Co_2N at different potentials in N_2-and Ar-saturated 0.1 M Na_2SO_4 (bars represent standard deviation).

c, Y_{NH3} and FEs of GDY/Co_2N and some reported excellent electrocatalysts performed in neutral conditions. **d**, Cycling test of GDY/Co_2N at -0.6 V versus SCE in 0.1 M Na_2SO_4.

In order to gain deeper understanding on the origin of the ECNRR performance of GDY/Co_2N, the electrochemical impedance spectroscopy (EIS, Supplementary Fig.26) was measured and fitted by using an equivalent circuit model (R(QR)(QR)) containing solution resistance (R_s), charge transfer resistance (R_{ct}) and adsorption resistance (R_{ad}). Compared with all reference samples, the GDY/Co_2N possessed the lowest R_s and R_{ct} values in both 0.1 M HCl (R_s = 10.07 Ω, R_{ct} = 0.75 Ω) and 0.1 M Na_2SO_4 (R_s = 8.69 Ω, R_{ct} = 2.5 Ω), indicating the most favorable charge transfer kinetics of GDY/Co_2N during the ECNRR process, which is beneficial to the improvement of the catalytic activity. We further measured the electrochemically active surface area (ECSA) of the samples. Electrochemical measurements showed that GDY/Co_2N had a largest capacitance of 7.17 mF cm^{-2}, approximately 1.65 times that of Co_2N (4.35 mF cm^{-2}), indicating that the former had larger ECSA (Supplementary Fig.27). Results above certificated that incorporation of GDY and Co_2N could facilitate the charge transfer behavior and offer more electrochemical active sites, which resulted in great improvements of ECNRR catalytic performances.

Conclusion

In summary, self-standing GDY/Co_2N was successfully synthesized through a facile and scalable method. It has been demonstrated to be a promising catalyst for ECNRR with 100% selectivity and high ammonia yield rate and Faradaic efficiency, which is favorable compared to previously reported electrocatalysts. Our results showed that the GDY layer at the interface region play a significant role for promoting electron-transfer towards N_2. Meanwhile, the GDY layer uniquely modifies the Co_2N surface states for acting as electron-pumping center, which drives the interface Co-sites effectively transfer electrons from Co_2N towards GDY layer. And the introduction of GDY could generate more active sites and promote the charge transfer between metal species and GDY, which are beneficial to the improvement of the

ECNRR performances. The overall interface exhibits an important p-d coupling for N_2-fixation, which reflects a subtle volcano-plot showing a positive correlation between catalytic and electronic activities. Such interplay suggests an innovative strategy and path towards improving electrochemical based N-reduction performance. Ultimately, such new graphdiyne-based electrocatalyst supplies an attractive prospect for the carbon-free ammonia production.

Data availability

The data related to this study are available from the authors upon reasonable request.

References

1. Chen, J. G. et. al. Beyond fossil fuel–driven nitrogen transformations. *Science*. **360**, eaar6611 (2018).
2. Hao, Y. C. et. al. Promoting nitrogen electroreduction to ammonia with bismuth nanocrystals and potassium cations in water. *Nat. Catal*. **2**, 448-456 (2019).
3. Deng, J., Iñiguez, J. A., Liu, C. Electrocatalytic nitrogen reduction at low temperature. *Joule.* **2**, 846-856 (2018).
4. Singh, A. R. et. al. Electrochemical ammonia synthesis-the selectivity challenge. *ACS Catal*. **7,** 706-709 (2017).
5. Yang, X. et. al. Mechanistic insights into electrochemical nitrogen reduction reaction on vanadium nitride nanoparticles. *J. Am. Chem. Soc*. **140**, 13387-13391 (2018).
6. Ren, X. et. al. Electrochemical N_2 fixation to NH_3 under ambient conditions: Mo_2N nanorod as a highly efficient and selective catalyst. *Chem. Commun.* **54**, 8474-8477 (2018).
7. Chen, P. et. al. Interfacial engineering of cobalt sulfide/graphene hybrids for highly efficient ammonia electrosynthesis. *Proc. Natl. Acad. Sci. USA*. **116,** 6635-6640 (2019).
8. Licht, S. et. al. Ammonia synthesis by N_2 and steam electrolysis in molten hydroxide suspensions of nanoscale Fe_2O_3. *Science*. **345**, 637-640 (2014).
9. Chen, S. et. al. Electrocatalytic synthesis of ammonia at room temperature and atmospheric pressure from water and nitrogen on a carbon-nanotube-based electrocatalyst. *Angew. Chem. Int. Ed*. **56**, 2699-2703 (2017).
10. Cui, X., Tang, C., Zhang, Q. A review of electrocatalytic reduction of dinitrogen to ammonia under ambient conditions. *Adv. Energy Mater.* **8,** 1800369 (2018).

11. Li, S. J. et. al. Amorphizing of Au nanoparticles by CeOx–RGO hybrid support towards highly efficient electrocatalyst for N_2 reduction under ambient conditions. *Adv. Mater*. **29**, 1700001 (2017).
12. Hui, L. et. al. Highly efficient and selective generation of ammonia and hydrogen on a graphdiyne-based catalyst. *J. Am. Chem. Soc.* **141**, 10677-10683 (2019).
13. Geng, Z. et. al. Achieving a record-high yield rate of 120.9 μg h^{-1} $mg_{cat.}^{-1}$ for N_2 electrochemical reduction over Ru single-atom catalysts. *Adv. Mater*. **30**, 1803498 (2018).
14. Nishibayashi, Y. Recent progress in transition-metal-catalyzed reduction of molecular dinitrogen under ambient reaction conditions. *Inorg. Chem*. **54**, 9234-9247 (2015).
15. Zhao, J., Chen, Z. Single Mo atom supported on defective boron nitride monolayer as an efficient electrocatalyst for nitrogen fixation: A computational study. *J. Am. Chem. Soc*. **139**, 12480-12487 (2017).
16. Li, G. et. al. Architecture of graphdiyne nanoscale films. *Chem. Commun.* **46**, 3256-3258 (2010).
17. Xue, Y. et. al. 2D graphdiyne materials: challenges and opportunities in energy field. *Sci China Chem*. **61**, 765-786 (2018).
18. Gao, X. et. al. Graphdiyne: Synthesis, properties, and applications. *Chem. Soc. Rev*. **48,** 908-936 (2019).
19. Li, Y. Design and self-assembly of advanced functional molecular materials—from low dimension to multi-dimension. *Sci. Sin. Chim*. **47,** 1045-1056 (2017).
20. Xue, Y. et. al. Self-catalyzed growth of Cu@graphdiyne core shell nanowires array for high efficient hydrogen evolution cathode. *Nano Energy*. **30,** 858-866 (2016).
21. Xue, Y. et. al. Anchoring zero valence single atoms of nickel and iron on graphdiyne for hydrogen evolution. *Nat. Commun*. **9,** 1460 (2018).
22. Yu, H. et. al. Efficient hydrogen production on a 3D flexible heterojunction material. *Adv. Mater*. **30,** 1707082 (2018).
23. Zhou, J. et. al. Synthesis of graphdiyne nanowalls using acetylenic coupling reaction. *J. Am. Chem. Soc*. **137,** 7596-7599 (2015).
24. Sun, M. et. al. Mapping of atomic catalyst on graphdiyne. *Nano Energy* **55**, 754–763 (2019).
25. Kan, X. et. al. Interfacial synthesis of conjugated two-dimensional N-graphdiyne. *ACS Appl. Mat. Interfaces*. **10,** 53-58 (2018).
26. Qi, H. T. et. al. Graphdiyne oxides as excellent substrate for electroless deposition of Pd clusters with high catalytic activity. *J. Am. Chem. Soc*. **137,** 5260-5263 (2015).

27. Gao, X. et. al. Direct synthesis of graphdiyne nanowalls on arbitrary substrates and its application for photoelectrochemical water splitting cell. *Adv. Mater*. **29,** 1605308 (2017).
28. Li, J. et. al. Architecture of beta-graphdiyne-containing thin film using modified glaser-hay coupling reaction for enhanced photocatalytic property of TiO_2. *Adv. Mater*. **29**, 1700421 (2017).
29. Zhao, Y. et. al. Graphdiyne: recent achievements in photo- and electrochemical conversion. *Adv. Sci.* **5**, 1800959 (2018).
30. Zuo, Z. et. al. Synthesis and applications of graphdiyne-based metal-free catalysts. *Adv. Mater*. **31**, 1803762 (2019).
31. Huang, C. et. al. Progress in research into 2D graphdiyne-based materials. *Chem. Rev*. **118**, 7744-7803 (2018)
32. Li, Y. et. al. Graphdiyne and graphyne: from theoretical predictions to practical construction. *Chem. Soc. Rev*. **43**, 2572-2586 (2014).
33. Gao, X. et. al. Ultrathin graphdiyne film on graphene through solution-phase van der Waals epitaxy. *Sci. Adv*. **4**, eaat6378 (2018).
34. Zhang, B. et. al. Homogeneously dispersed, multimetal oxygen-evolving catalysts. *Science*. **352**, 333-337 (2016).
35. Zhao, S. et. al. Ultrathin metal–organic framework nanosheets for electrocatalytic oxygen evolution. *Nat. Energy*. **1**, 16184 (2016).
36. Watt, G.W., Chrisp, J. D. Spectrophotometric method for determination of hydrazine. *Anal. Chem*. **24**, 2006-2008 (1952).
37. Qiu, W. B. et. al. High-performance artificial nitrogen fixation at ambient conditions using a metal-free electrocatalyst. *Nat. Commun.* **9**, 3485 (2018).
38. Zhang, L. L. et. al. Ammonia synthesis under ambient conditions: selective electroreduction of dinitrogen to ammonia on black phosphorus nanosheets. *Angew. Chem. Int. Ed.* **58**, 2612-2616 (2019).
39. Wang, J. et. al. Ambient ammonia synthesis via palladium-catalyzed electrohydrogenation of dinitrogen at low overpotential. *Nat. Commun.* **9**, 1795 (2018).
40. Cheng, H. et. al. Molybdenum carbide nanodots enable efficient electrocatalytic nitrogen fixation under ambient conditions. *Adv. Mater.* 1803694 (2018).
41. Li, X. H. et. al. Boosted electrocatalytic N_2 reduction to NH_3 by defect-rich MoS_2 nanoflower. *Adv. Energy Mater.* **8**, 1801357 (2018).
42. Zhang, Y. et. al. High-performance electrohydrogenation of N_2 to NH_3 catalyzed by multishelled hollow Cr_2O_3 microspheres under ambient conditions. *ACS Catal.* **8**, 8540-

8544 (2018).

Acknowledgements

This work was supported by the National Nature Science Foundation of China (21790050 and 21790051), the National Key Research and Development Project of China (2016YFA0200104 and 2018YFA0703501), the Key Program of the Chinese Academy of Sciences (QYZDY-SSW-SLH015), and the Early Career Scheme (ECS) fund (Grant No.: PolyU 253026/16P) from the Research Grant Council (RGC) in Hong Kong. We would like to thank the XAFS station (beam line 1W1B) of the Beijing Synchrotron Radiation Facility for the XAS measurements.

Author contributions

Y.L. conceived the research, reviewed and edited this manuscript. Y.F. synthesized the catalysts, performed the experiments, and anlaysed the data. Y.X. directed the overall projected, organized the data, and wrote the paper. B.H. conducted the theoretical calculations. H.Y., L.H., Y.L., C.X., C.Z., D.Z, and Z.W. gave useful help.

Competing interests

The authors declare no competing interests.